Decay of Solar Pores Driven by Small-scale Magnetic Reconnection Episodes

Zhike Xue[1,2,3] , Xiaoli Yan[1,3] , Liheng Yang[1,2,3] , Jie Chen[2] , Jincheng Wang[1,3] , Qiaoling Li[4] , and Li Zhao[1,3]

[1] Yunnan Observatories, Chinese Academy of Sciences, Kunming, Yunnan 650216, People's Republic of China; zkxue@ynao.ac.cn
[2] CAS Key Laboratory of Solar Activity, National Astronomical Observatories, Beijing 100012, People's Republic of China
[3] Center for Astronomical Mega-Science, Chinese Academy of Sciences, Beijing 100012, People's Republic of China
[4] Department of Physics, Yunnan University, Kunming, Yunnan 650091, People's Republic of China

Abstract

We present the relationships between the disappearances of two small pores, magnetic cancellations, and magnetic reconnection episodes in the NOAA AR 12778 on 2020 October 26 with high-resolution observations of the New Vacuum Solar Telescope and the Solar Dynamics Observatory. Two emerging positive polarities (P1 and P2) approach a negative polarity (N1) with velocities of 0.26 and 0.42 km s^{-1}, respectively. Then, two small-scale magnetic reconnection episodes occur between a series of magnetic loops that are rooted in these polarities. The reconnection inflow velocities are around 4.0 km s^{-1} which is faster than the movements of P1 and P2. Compared with the first magnetic reconnection episode, more magnetic free energy is released in the second reconnection episode due to the greater magnetic strength of P2. Subsequently, magnetic cancellation occurs first between P1 and N1, and then between P2 and N1. At the same time, the pores S1 (N1) and S2 (P2) decay and disappear. The area decay rate of the small pore S2 is estimated to be 7.3 Mm^2 hr^{-1}, which is larger than previously reported cases. And the flux decay rate of S2 is 5.1×10^{19} Mx hr^{-1}, similar to the results obtained in the larger sunspots. We conclude that the magnetic reconnection episodes may be caused by both the movement of the magnetic polarities and the plasma dynamics themselves. The decay and disappearance of the small pores and the polarities are driven by magnetic reconnection episodes and then flux submergence. We suggest that a magnetic reconnection episode is a more efficient mechanism for the disappearance of solar pores.

Unified Astronomy Thesaurus concepts: Solar magnetic reconnection (1504); Solar magnetic fields (1503); Sunspots (1653); Solar activity (1475)

Supporting material: animations

1. Introduction

A magnetic reconnection episode is a fundamental and important physical process in the release of magnetic energy. In solar physics, a magnetic reconnection episode is a hot topic and it is often considered to be a key feature of solar eruptions, such as flares, coronal mass ejections, jets, and so on (Sturrock 1966; Shibata et al. 1992; Xue et al. 2017, 2020; Yan et al. 2018; Xing et al. 2020; Li et al. 2021b; Shen 2021). Until now, a lot of the observational evidence of magnetic reconnection episodes has been provided by ground-based and spaceborne solar telescopes (Yokoyama et al. 2001; Asai et al. 2004; Takasao et al. 2012; Xue et al. 2016, 2019). Even so, very few cases with a clear reconnection episode are reported since the observations are affected by the projection effect or the magnetic reconnection episode lasts for a short time. So far, it is not clear how magnetic reconnection episodes are triggered and how the magnetic energy is released. Recently, Xue et al. (2021) statistically studied six small-scale magnetic reconnection events in the lower atmosphere of the Sun and found that even if the magnetic reconnection episodes occur in different active regions (ARs), their physical parameters are statistically correlated. In particular, when the separatrix angle is close to 90°, the separatrix jet and the outflow reach their maximum velocities and the reconnection rate decreases as the inflow velocity increases. Recently, Ni et al. (2020) and Lee & Lee (2020) reviewed the improving theory and observation of magnetic reconnection episodes, respectively.

The evolution of the AR plays a key role in understanding the origin of the solar magnetic fields and the solar cycle and sunspot decay is one of the very important processes during sunspot evolution. Although sunspot decay has been studied for many years, its physical mechanism is still a mystery. Sunspot decay is often considered to include the continuum area decay and magnetic decay and the latter is more important to reveal its mechanism (see Martínez Pillet 2002). Various models of sunspot decay have been proposed in recent decades, for example, self-similar-spot, turbulent diffusion, turbulent erosion, and universal parabolic (Gokhale & Zwaan 1972; Meyer et al. 1974; Martínez et al. 1993; Petrovay & Moreno-Insertis 1997). The former belongs to the fast mode and the last three models are classified as gradual mode (van Driel-Gesztelyi 1998). The obvious observational characteristics of sunspot decay include the moat region, moat flow and moving magnetic features (MMFs), and the light bridge (Harvey & Harvey 1973; Meyer et al. 1974; Leka 1997).

In recent years, sunspot decay has been investigated in detail using high-resolution observation data. Benko et al. (2018) found that the area and magnetic flux of the umbra of a decaying sunspot decrease linearly, and their decay rates are estimated to be 0.2 and 4.5×10^{18} Mx hr^{-1}, while for the penumbra, a convex decay of its area and a linear decay of its magnetic flux are found. Verma et al. (2018) investigated the decay process of a leading sunspot in detail and found that the new emerging flux system may affect the penumbral decay. The decay rates of the flux and area are 1.4×10^{19} Mx hr^{-1} and 0.42 Mm^2 hr^{-1}, respectively. Murabito et al. (2021) studied the decay process of a penumbra in the central region of NOAA 12585 with an average rate of 7.1×10^{19} Mx hr^{-1}. They concluded that the interaction between MMFs and the penumbra may result in penumbral decay. Li et al. (2019) investigated three parts of NOAA 12673 and proposed that
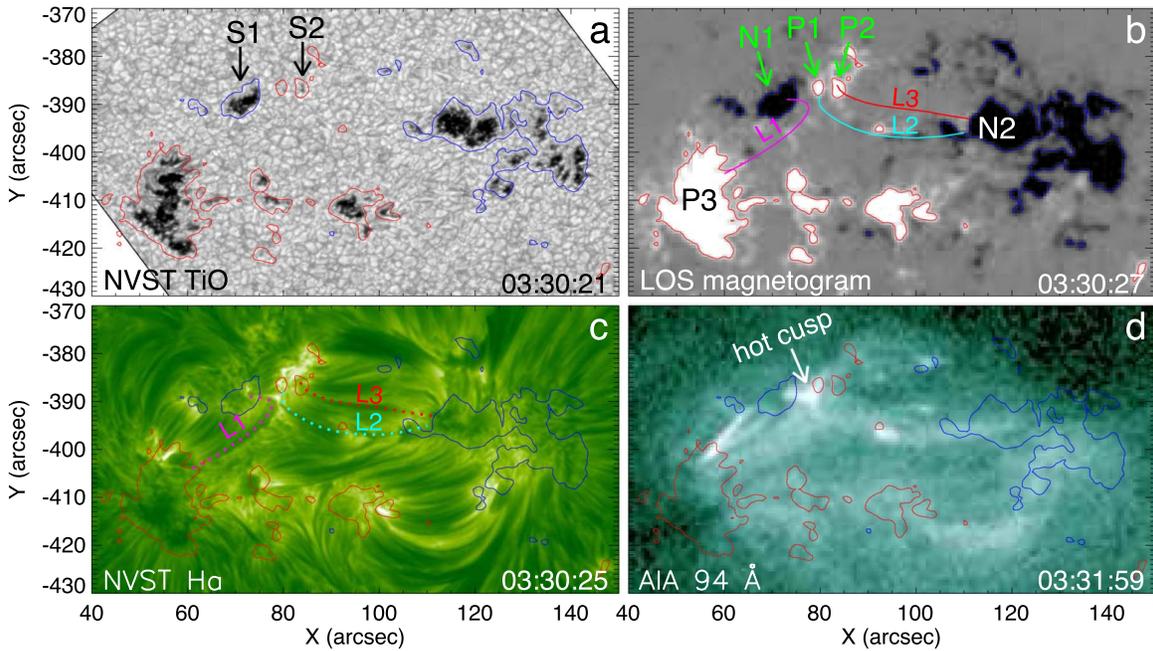
Figure 1. Overview of the NOAA AR 12778. (a) The NVST TiO image showing the sunspots and pores and two small pores S1 and S2 are marked by the black arrows. (b) The HMI LOS magnetogram of AR 12778 and the main polarities (P3 and N2) and several small polarities (N1, P1, and P2). (c) The NVST Hα image in which three sets of magnetic loops (L1, L2, and L3) are marked by the pink, cyan, and red lines, respectively. (d) The AIA 94 Å image showing a bright cusp-shaped structure indicated by the white arrow. The red and blue contours of the SDO/HMI magnetogram with levels of ±300 G indicate positive and negative polarities, respectively.

the umbra and penumbra have different decay mechanisms. Li et al. (2021b) studied statistically the decay of eight α-configuration sunspots and found that the area and total magnetic flux of α sunspots show a near-linear decrease. They reported that the decay rate of the sunspot area ranges from 1.1 to 3.3 $Mm^2\,hr^{-1}$ and the sunspot flux decay rate is between 5.9×10^{18} and 20.3×10^{18} $Mx\,hr^{-1}$.

In this Letter, we present an observational case of the decay and disappearance of solar pores and related magnetic polarities driven by two small-scale magnetic-reconnection episodes. In Section 2, we display the observations and the analysis methods of high-resolution data. The results are described in Section 3. Discussions and summary are presented in Section 4.

2. Observations

The high-resolution data are observed by the New Vacuum Solar Telescope (NVST; Liu et al. 2014) and the Solar Dynamic Observatory (SDO; Pesnell et al. 2012). The NVST is a one-meter solar telescope located at Fuxian Solar Observatory of Yunnan Observatories, Chinese Academy of Sciences (CAS). Its purpose is to study the fine structure and small-scale activities in the lower atmosphere of the Sun (Yan et al. 2020), thus it provides high-resolution images of the photosphere and chromosphere in the TiO (7058 Å with a bandwidth of 10 Å) and Hα (6562.8 Å with a bandwidth of 0.25 Å) wave bands, respectively. The spatial resolution and temporal resolution of the NVST TiO image are 0″.105 and 30 s, respectively, while the NVST Hα image with a spatial resolution of 0″.33 is reconstructed every 12 s. On 2020 October 26, the NVST observes the Sun in the TiO wave band and Hα line center except for the wings of the Hα line, thus the Dopplergrams in the chromosphere are not obtained. The extreme ultraviolet data are used to demonstrate high-temperature structures, which are obtained by the Atmospheric Imaging Assembly (AIA; Lemen et al. 2012) on board SDO. The

continuum images and the line-of-sight (LOS) magnetograms provided by the Helioseismic and Magnetic Imager (HMI; Scherrer et al. 2012) on board SDO and the vector magnetic fields formatted in the Spaceweather HMI Active Region Patch (SHARP; Bobra et al. 2014) are used to show the magnetic configuration. The SHARP data include 16 parameters that are calculated using HMI vector magnetic-field data with a 12 minute cadence. Among them, B_p is the ϕ component of the heliographic Cylindrical Equal-Area (CEA) vector magnetic field in the direction of solar rotation, and B_r is the radial (out of photosphere) component of the CEA vector magnetic field. Based on the SHARP data, the pixels where $B_p < 0$ G and $B_r > 200$ G in the focused positive polarities are counted and B_r is set to be equal to 200 G to avoid the influence of other polarities on the results. Furthermore, the coronal magnetic field is obtained by extrapolating the SHARP vector magnetograms based on a non-linear force-free field (NLFFF) method (Wiegelmann 2004; Wiegelmann et al. 2006). The temperatures are estimated through differential emission measure (DEM) analysis (Cheng et al. 2012; Hannah & Kontar 2012). Additionally, running-difference images of NVST Hα data are computed by subtracting the images 60 s earlier.

3. Results

On 2020 October 26, the AR NOAA 12778 is observed by the NVST. It is located at S25W06 and is a developing active region (see Figures 1(a) and (b)). It consists of two main sunspot groups and some fragments, including small sunspots and pores. The leading sunspot has a negative polarity (named N2) and the following sunspot corresponds to a positive polarity (P3), respectively. The two main sunspots gradually move away from each other, and several small pores emerge in the middle region between the two main sunspots. Among them, two small pores are focused on, which are labeled S1 and
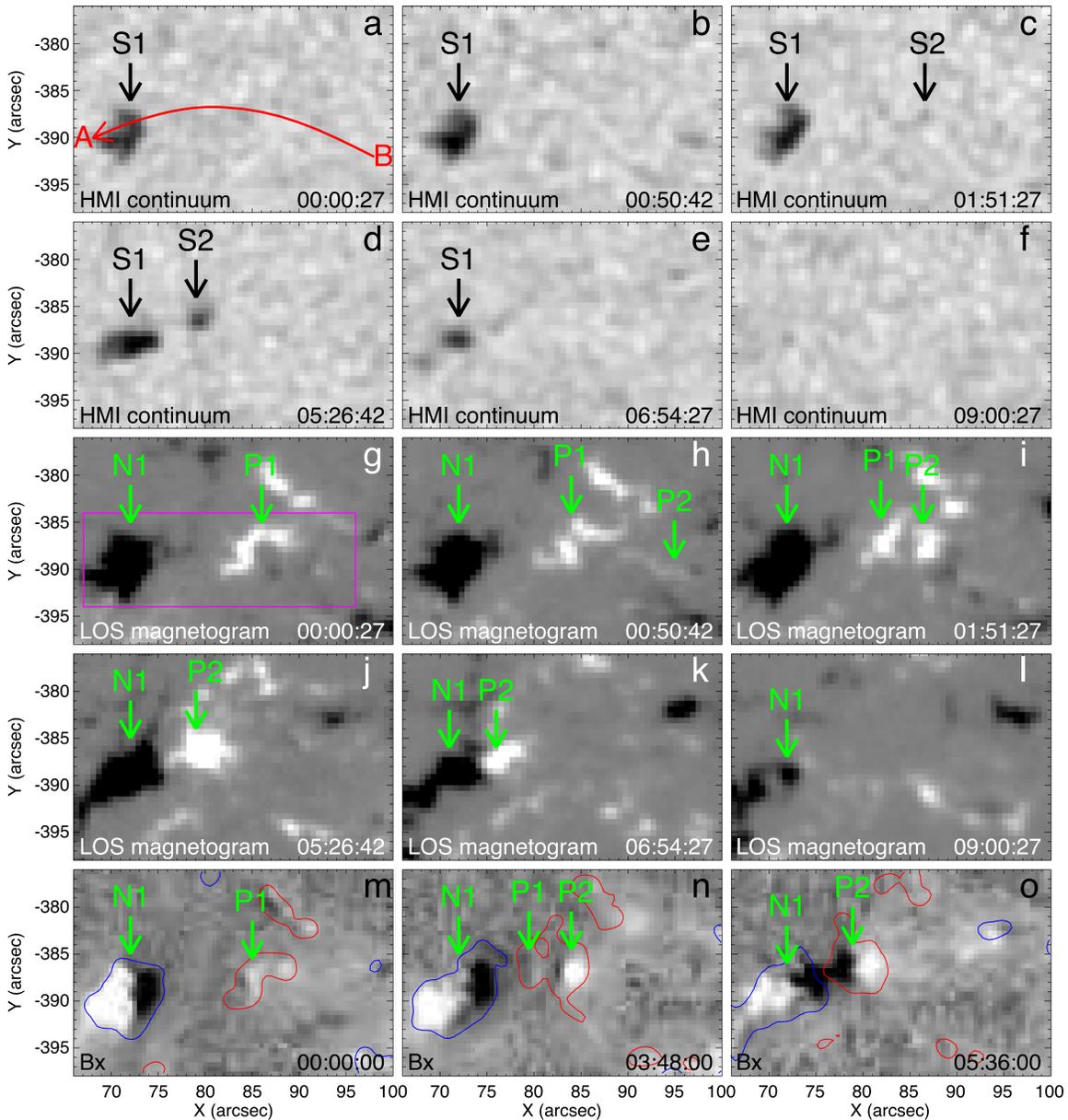
Figure 2. Evolution of the focused pores and polarities. ((a)–(f)) The HMI continuum images displaying the appearance and disappearance of S1 and S2. ((g)–(l)) The HMI LOS magnetograms showing the evolutions of N1, P1, and P2. ((m)–(o)) B_p of the SHARP vector magnetic fields. The red and blue contours of B_r with levels of ± 200 G indicate positive and negative values, respectively. An animation with the SDO/HMI continuum images (panels (a) and (c)) and the magnetograms (panels (b) and (d)) is available. The animation covers all of the images from 00:00:27 UT to 09:59:42 UT on 2020 October 26. The duration of the animation is 13 s. The blue rectangle in the panel (a) indicates the field of view (FOV) of the right panels.

(An animation of this figure is available.)

S2 in Figure 1(a). In the HMI magnetogram (Figure 1(b)), S1 corresponds to a negative polarity N1, and S2 has a positive polarity P2. Between N1 and P2, another small positive polarity P1 is observed. However, in the NVST TiO image, there is no pore corresponding to P1. It is noted that P1 and P2 first emerge near N2 and then move away from N2, while N1 emerges near P3 and then moves northwest. In the NVST Hα image (Figure 1(c)), there are many chromospheric fibrils that show dark curve structures, and they are usually called arch-filament systems (AFSs, e.g., Bruzek 1980; Murabito et al. 2017; González Manrique et al. 2018). Previous studies have shown that AFSs often reconnect with the ambient fields (e.g., Tarr et al. 2014; Su et al. 2018). Three sets of loops are indicated by the dotted lines and are labeled as L1, L2, and L3,

respectively. It is found that L1 connects the polarities P3 and N1. The right footpoints of L2 and L3 are both rooted in N2, while the left footpoints are rooted in P1 and P2, respectively. In the AIA 94 Å image (Figure 1(d)), a hot cusp structure is observed near the small pores, and it is often thought to be the characteristic of a magnetic reconnection episode. In fact, we observe two small-scale magnetic reconnection episodes between L1 and L2 and between L1 and L3 in this region which begin at about 01:44 UT and 04:10 UT, respectively (see the following paragraphs).

Figure 2 shows the evolution of the small pores (S1 and S2) and the related polarities (N1, P1 and P2). In the initial stage, S1 is first observed to appear in the HMI continuum image (Figure 2(a)), while the related polarity N1 can also be seen in
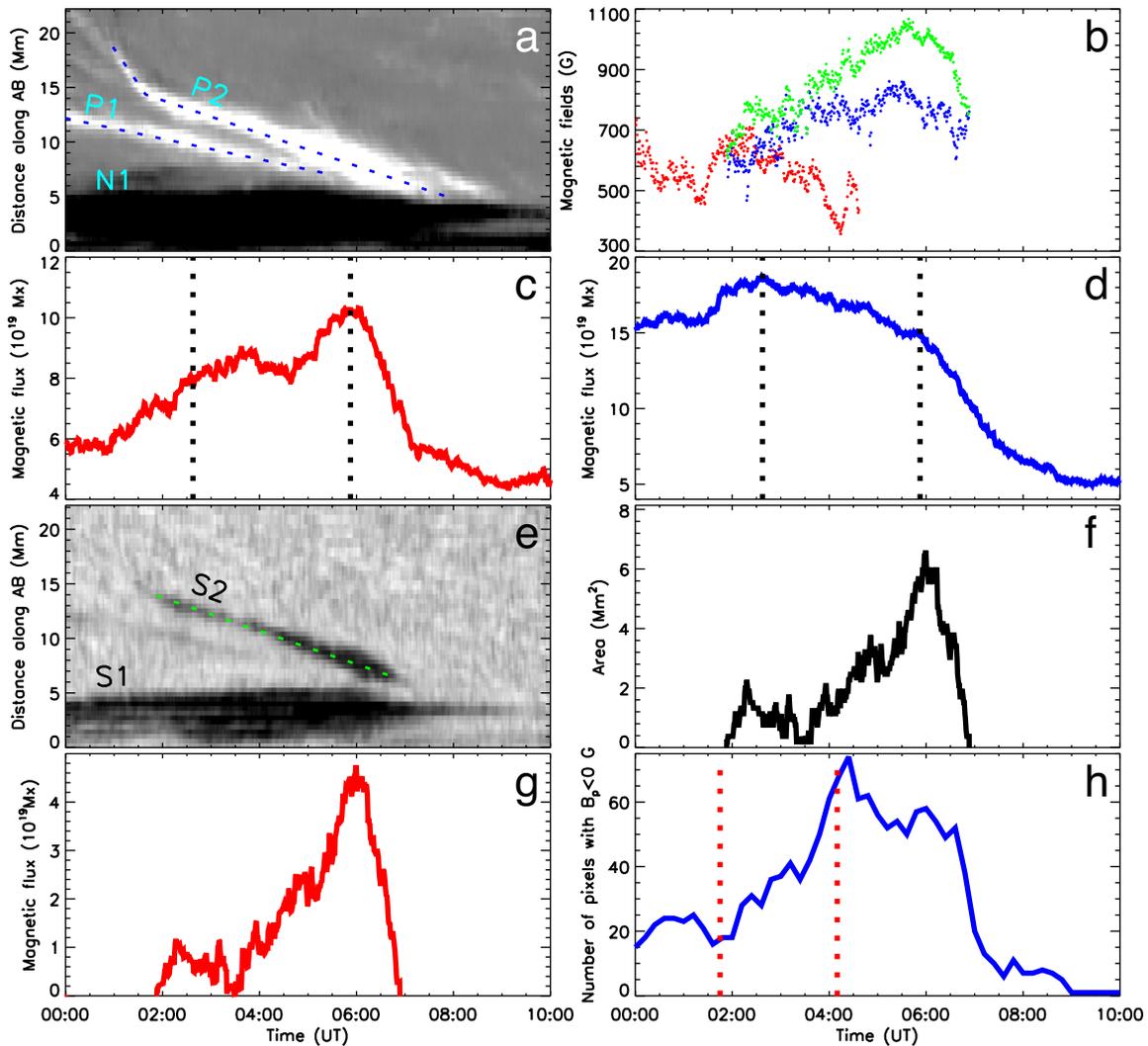
3

Figure 3. ((a), (e)) Time–distance diagrams made along the slice AB in Figure 2(a) using LOS magnetograms and HMI continuum images. (b) The magnetic field strength of P1 and P2. The green, blue, and red dots represent the maximum and the average strength of LOS magnetic fields in S2 and the maximum value of LOS magnetic fields in P1, respectively. ((c), (d), and (h)) The positive and negative magnetic flux and the number of the pixels with $B_p < 0$ and $B_r > 200$ G in the region marked by the pink rectangle in Figure 2(g). ((f), (g)) The evolution of the area and magnetic flux of S2. The black dotted lines in panels (c) and (d) indicate the onsets of two magnetic cancellations, while the red dotted lines in panel (h) indicate the onsets of two magnetic reconnection episodes.

the HMI LOS magnetogram at the same time (Figure 2(g)). In addition, another polarity P1 also appears in the magnetogram but no corresponding pore. Then, it is found that P1 approaches N1 with a velocity of 0.26 km s^{-1} (Figure 3(a)) and gradually becomes smaller and smaller until it disappears from the magnetogram at about 05:26 UT (see Figure 2(j) and the attached movie of Figure 2). The maximum LOS magnetic field strength in P1 is measured and displayed in Figure 3(b) using red dots, which is from 734 to 357 G with a mean value of 560 G. Furthermore, the positive and negative magnetic fluxes in the box marked by the pink rectangle in Figure 2(g) are calculated and shown in Figures 3(c) and (d), respectively. The negative magnetic flux begins to decrease at 02:37 UT when it has a maximum value of 18.7×10^{19} Mx. It slowly decreases with a rate of 1.2×10^{19} Mx hr^{-1} until 05:26 UT when its value reaches 15.2×10^{19} Mx. While the positive magnetic flux does not decrease because P2 emerges in the box at the same time. It should be noted that in the box, the negative magnetic flux is from N1. This indicates that magnetic

cancellation may take place between N1 and P1 during the disappearance of P1.

The HMI magnetograms also show that P2 begins to emerge obviously at around 00:50 UT (see Figure 2(h)). Then it quickly approaches N1 along the path BA (the red line in Figure 2(a)) with a velocity of 1.79 km s^{-1} at first, and then it suddenly decelerates to 0.42 km s^{-1} at 01:39 UT (Figure 3(a)). While the corresponding pore S2 starts to be observed in the HMI continuum image at around 01:51 UT, which is nearly 1 hr later than P2. Similarly, it moves to S1 with a velocity of 0.42 km s^{-1} (see Figure 3(e)). When S2 approaches S1, it starts to decay gradually and is not found in the HMI continuum image at 06:54 UT (Figure 2(e)). At the same time, S1 becomes smaller and smaller and finally disappears at about 09:00 UT (Figure 2(f)). The evolutionary process of P2 and N1 is similar (see Figures 2(h)–(l)), but they disappear later than their corresponding pores.

In order to study the detailed process of the disappearance of S2, its magnetic field strength, area, and magnetic flux are obtained and displayed in Figures 3(b), (f), and (g), respectively. The maximum and average magnetic field strength in S2 at each

observational time is calculated and shown in Figure 3(b) with green and blue dots, respectively. It is found that the average magnetic field strength is from 468 to 861 G, while the maximum magnetic field strength is from 608 to 1067 G which is greater than that in P1. Furthermore, the area of S2 increases to a local maximum (2.8 Mm^2) at 02:18 UT, then becomes smaller and smaller until 03:29 UT. After that, it increases again and reaches its global maximum value (6.6 Mm^2) at 05:59 UT. Next, S2 quickly decays with a decay rate of 7.3 Mm^2 hr^{-1} until 06:54 UT when it disappears completely. The magnetic flux in S2 (Figure 3(g)) shows the similar evolution as the area of S2. The maximum magnetic flux reaches 4.8×10^{19} Mx and its decrease rate is 5.1×10^{19} Mx hr^{-1}.

Similarly, another magnetic cancellation occurs between P2 and N1, which begins at 05:53 UT (see Figures 3(c) and (d)). The positive and negative magnetic fluxes decrease simultaneously. In the initial stage of second magnetic cancellation, they decrease quickly and their rates are 3.6×10^{19} Mx hr^{-1} and 4.5×10^{19} Mx hr^{-1}, respectively. However, after 07:17 UT, the flux cancellation rates become 0.54×10^{19} Mx hr^{-1} and 1.8×10^{19} Mx hr^{-1}, respectively. It is found that the flux cancellation rate between P2 and N1 is higher than the first flux cancellation between P1 and N1, and more magnetic flux removes during the latter magnetic cancellation.

Additionally, it is observed that B_p of most pixels in P1 and P2 is positive in the initial stage (Figures 2(m) and (n)). Then the number of the pixel with negative B_p increase (Figures 2(m)–(o)). Since the magnetic polarities N1, P1, P2, and N2 are almost at the same latitude, the inclination directions at the footpoints of the magnetic loops connecting these magnetic polarities are also almost at the latitude (see also the results of the NLFFF, Figures 4(k)–(n)). When the magnetic reconnection episodes result in the exchange of their footpoints, for the magnetic loops rooted in P1 and P2, their connectivity is mainly converted from the west to the east. In other words, the change in the number of the pixel where $B_p < 0$ G in P1 and P2 indicates the change of the footpoints due to magnetic reconnection episodes. Therefore, the number of the pixel whose B_p is negative and B_r is greater than 200 G in the box marked in Figure 2(g) is counted at each observation time and presented in Figure 3(h). It is found that the number increases rapidly after 01:36 UT when the first magnetic reconnection episode starts to occur. Then it reaches maximum at 04:24 UT. After that, it decreases slowly until 05:36 UT and then decreases faster due to magnetic cancellations. It indicates that the footpoints of the magnetic loops are exchanged, which is caused by the magnetic reconnection episodes. Similarly, Hou et al. (2021) found that the transverse magnetic field in this region is enhanced.

Two small-scale magnetic reconnection episodes are clearly observed by the NVST and SDO during the decay of S1 and S2 (see Figure 4 and its attached movie). The reconnection inflows and outflows are indicated by the black and white arrows in the NVST Hα images (Figures 4(b) and (f)). The first magnetic reconnection episode occurs between L1 and L2 which are marked by the pink and cyan lines in Figure 4(b). These two sets of magnetic loops approach and interact with each other and then reconnect. A set of shorter magnetic loops which connect the polarities P1 and N1 (the yellow line in Figure 4(b)) and a set of longer loops which connect P3 and N2 (the green line in Figure 4(i)) form during this reconnection episode. The second magnetic reconnection episode occurs between L1 and L3 marked by the pink and red lines (Figure 4(f)), and results in the formation of another shorter loop connecting P2 and N1 (the yellow line in Figure 4(f)) and a longer loop connecting P3 and N2 (the green line in Figure 4(j)). Furthermore, two linear-bright structures are observed and indicated by the blue arrows in the AIA 171 Å images (Figures 4(c) and (g)), and they are often considered to be a current sheet. At the two ends of each current sheet, two bright cusp-shaped structures are found in the AIA 171 Å image (the black lines in Figures 4(c) and (g)). Furthermore, the cusp structures in the northeast can also be observed clearly in the AIA 94 Å image whose response temperature is higher (see Figures 4(d) and (h)).

In addition, the NLFFF extrapolations from two different views (top view in Figures 4(k) and (m) and side view in Figures 4(l) and (n)) reveal the magnetic topology during the magnetic reconnection episodes. In the first magnetic reconnection episode, the cyan and pink magnetic loops reconnect and the newly formed loops are marked by the green and yellow lines in Figures 4(k)–(l), while in the second magnetic reconnection episode, the reconnection episode occurs between the pink and red lines, and the newly formed magnetic loops are marked by the green and yellow lines in Figures 4(m)–(n). However, any magnetic loops connecting P1 and N1, or connecting P2 and N1 are not found before the magnetic reconnection episodes using the NLFFF method, and this confirms our observations.

Two time–distance diagrams (Figures 5(a) and (b)) are obtained along the line CD in Figure 4(b) to show the dynamic of the reconnection episodes. The reconnection inflows are clearly observed in the time–distance diagrams, and several typical inflows are indicated by the green lines. Their velocities are estimated to be from 4.0 to 4.4 km s^{-1} during the first reconnection episode and from 3.3 to 4.9 km s^{-1} during the second reconnection episode. These are similar to previous results in the solar lower atmosphere (e.g., Xue et al. 2019).

Furthermore, the 171 and 94 Å normalized intensities (Figure 5(c)) in the region marked by the white square in Figure 4(d) are obtained. We find that they almost maintain the same brightness before about 01:44 UT. After 01:44 UT when the first reconnection episode begins, the 171 Å intensity becomes larger and larger. However, the 94 Å images in this region still does not brighten significantly. At about 04:10 UT when the second reconnection episode starts, the 94 Å intensity begins to increase quickly. Similarly, the region in the 171 Å channel becomes brighter than before. They reached their maximum intensities at 06:32 UT (94 Å) and 06:40 UT (171 Å), respectively. Then they decrease rapidly to their initial intensities. Additionally, the average temperature (Figure 5(d)) in this region based on the DEM method shows that it has a value of around 1.1×10^6 K before 04:10 UT, even during the first magnetic reconnection episode. After that, the temperature rises rapidly, and this highest temperature can reach 4.07×10^6 K at 05:54 UT due to the second reconnection episode. From about 06:30 UT, the temperature decreases rapidly. It is believed that the energy release during the second reconnection episode is more efficient, and more magnetic energy is released due to stronger magnetic fields of P2.

4. Summary and Discussion

On 2020 October 26, a series of interrelated active events have been observed in the NOAA AR 12778, including the
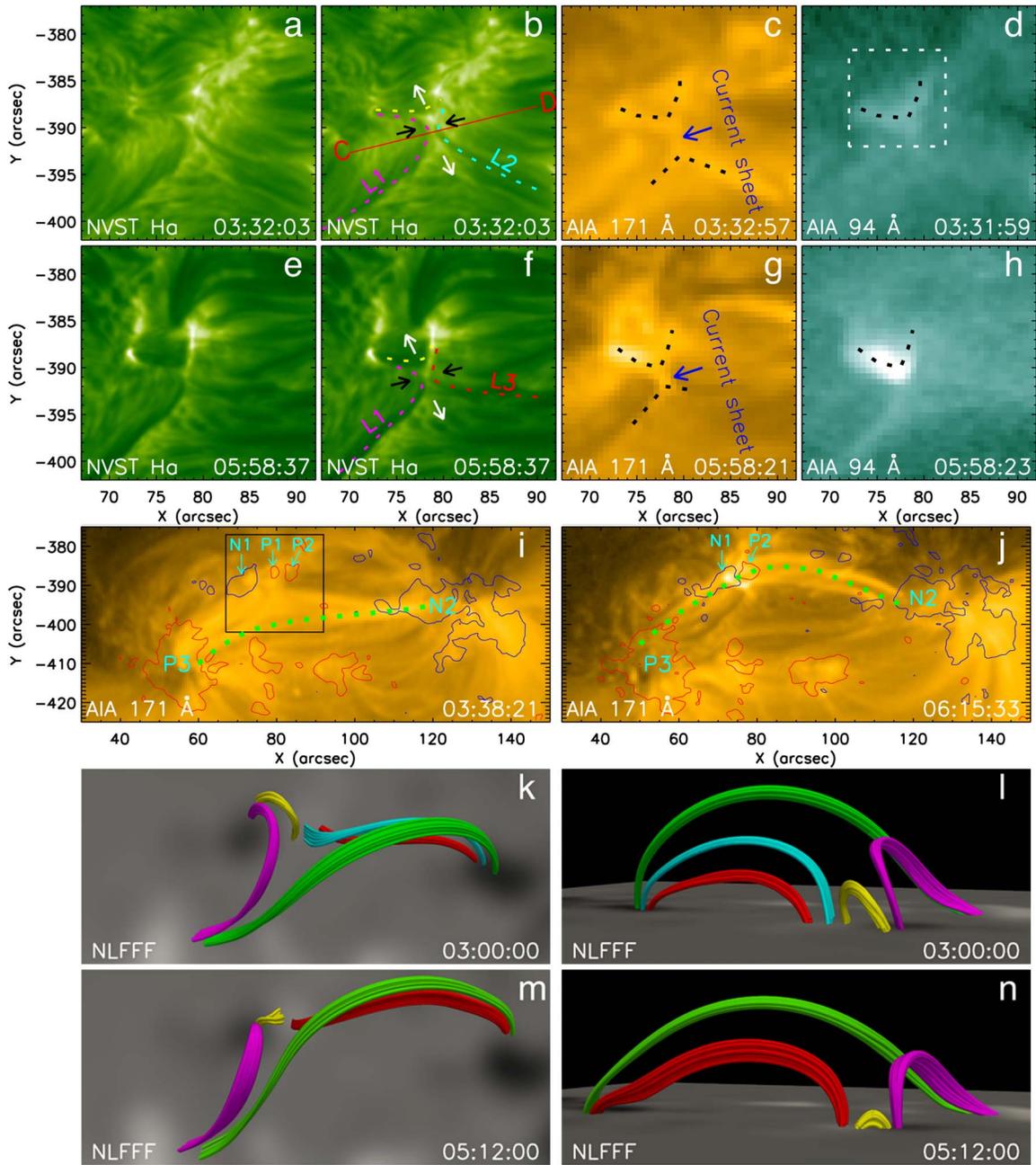
Figure 4. Observations of two magnetic reconnection episodes in NVST Hα images (panels (a), (b), (e) and (f)), AIA 171 Å images (panels (c), (g), and (i)–(j)), and AIA 94 Å images (panels (d) and (h)). The FOV of panels (a)–(h) is by the black square in panel (i). The inflows, outflows, and current sheets are marked by the black, white, and blue arrows. The pink, blue, and red dotted lines indicate the magnetic loops before the reconnection episodes, while the yellow and green lines indicate the newly formed magnetic loops. The hot cusp-shaped structures are marked by black dotted lines. The red and blue contours of the SDO/HMI magnetogram with levels of ±300 G indicate positive and negative polarities, respectively. In panels (k)–(n), 3D NLFFF configurations from two different views (top view in panels (k) and (m) and side view in panels (l) and (n)) during the magnetic reconnection episodes are shown. The pink, cyan, and red lines represent the magnetic loops before reconnection episodes, and the yellow and green lines show shorter and longer loops formed in the magnetic reconnection episodes. An animation of the NVST Hα (panels (a) and (c)) and SDO/AIA 171 Å (panels (b) and (d)) images, covering from 03:25:07 UT to 08:49:18 UT on 2020 October 26, is available. The duration of the animation is 28 s. The pink rectangle in the panel (a) indicates the FOV of the bottom panels.

(An animation of this figure is available.)

appearance and disappearance of the small pores and polarities, the magnetic reconnection episodes, and the magnetic cancellations. One small positive polarity P1 emerges first and then approaches the pre-existing negative pole N1 which corresponds to a small pore S1. However, no pores or sunspots are formed in P1 due to its lower magnetic strength. Another small positive polarity P2 which has a small pore S2 emerges

immediately afterward and then also moves closer to N1. Two magnetic reconnection episodes are recognized to occur between L1 and L2 and then between L1 and L3, respectively. The observational evidence includes the reconnection inflows with velocities from 3.3 to 4.9 km s^{-1}, the exchange of the footpoints of the magnetic loops, the newly formed loops, the current sheets and cusp-shaped structures, and brightening and
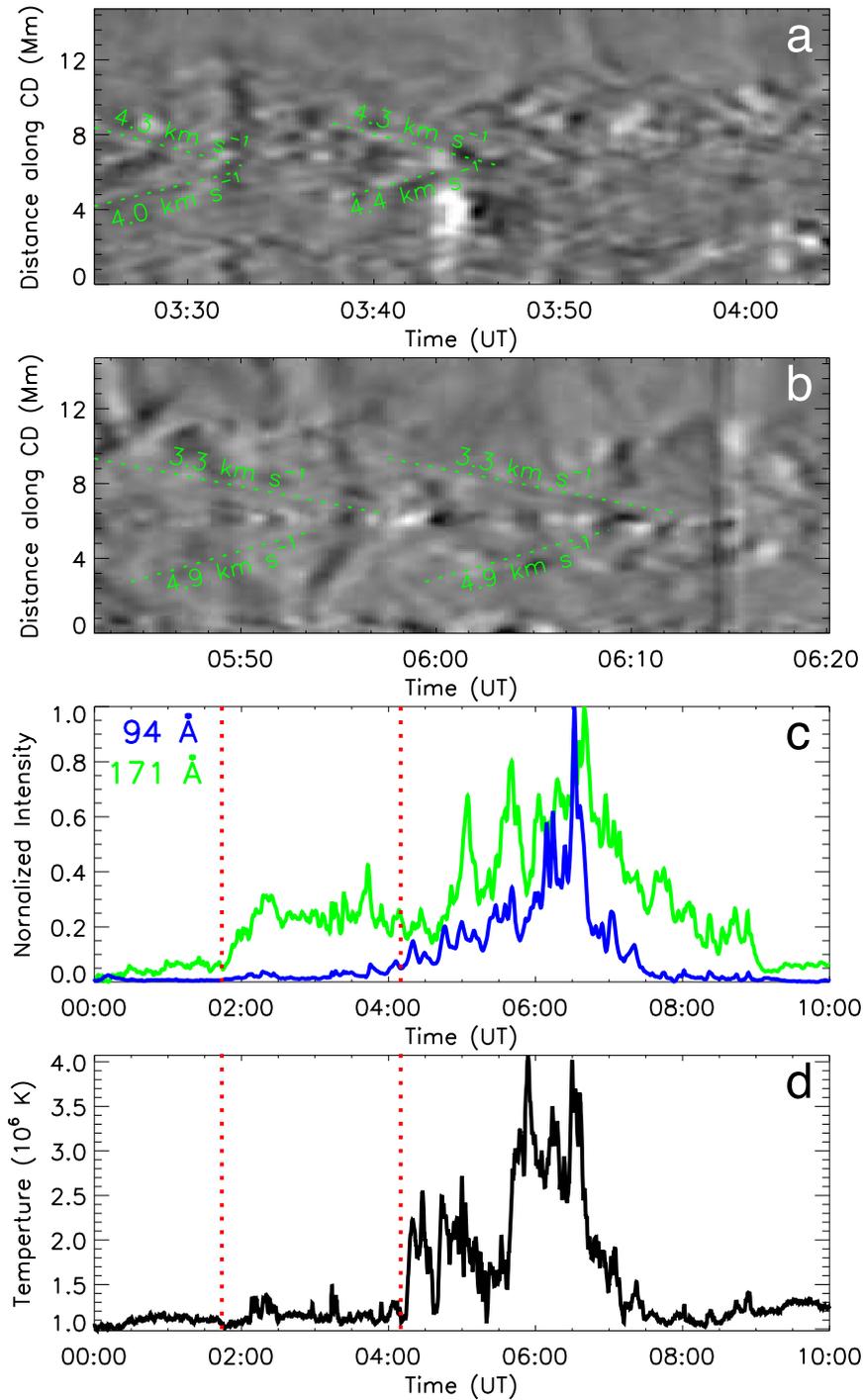
Figure 5. ((a)–(b)) Time–distance diagrams computed along the red line CD in Figure 4(b) and several typical inflows are marked by the green lines and their velocities are calculated. ((c)–(d)). The normalized intensity of the AIA 94 and 171 Å images and average temperature in the region are marked by the white square in Figure 4(d). The red dotted lines represent the onsets of two magnetic reconnection episodes.

heating in the reconnection site. After each reconnection episode, the magnetic cancellation occurs first between P1 and N1, and then between P2 and N1, accompanied by the disappearance of S1 and S2.

Before the reconnection episodes, the polarities P1 and P2 gradually move closer to N1, and thus they simultaneously pulled the magnetic loops L2 and L3 to approach L1 gradually because one footpoint of L2 and L3 is rooted in P1 and P2, respectively. Then two magnetic reconnection episodes occur due to the interaction between L2 and L1 and between L3 and

L1. Xue et al. (2018) reported a similar observation and suggested that a small-scale reconnection episode is driven by the movement of a small sunspot in the photosphere with a velocity of $0.29\,\mathrm{km\,s^{-1}}$. However, they did not obtain the velocities of reconnection inflows due to the relatively low temporal resolution of their observation data, and thus did not compare them with the velocity of the sunspot movement. In this event, the velocities of the polarities (0.26 and $0.42\,\mathrm{km\,s^{-1}}$) and the magnetic inflows (around $4\,\mathrm{km\,s^{-1}}$) are all calculated and the latter is about 10 times the former.

Furthermore, it is found that even if the magnetic polarity (e.g., N1) moves slowly, the corresponding magnetic loops can also quickly move to the reconnection site and interact with other loops. We conclude that the movements of the polarities provide the conditions for the occurrence of reconnection episodes and the intrinsic reason for triggering a magnetic reconnection episode may be determined by the properties of the plasma and the magnetic field itself. Although two types of magnetic reconnection episodes have been proposed, including spontaneous reconnection episodes and forced reconnection episodes (e.g., Treumann & Baumjohann 2015; Srivastava et al. 2019), how a magnetic reconnection episode is triggered is still a mystery. Yamada et al. (2010) believed that a magnetic reconnection episode is related to both local plasma dynamics in the reconnection region and global boundary conditions. And our observations confirm their perspective to a certain extent.

A magnetic reconnection episode is regarded as one mechanism of sunspot decay, however, the relationship between them is rarely reported. When explaining the disappearance of several δ sunspots and related flux cancellation, Wang (1992) proposed that a magnetic reconnection episode followed by flux submergence is the best explanation for the disappearance of δ sunspots. Liu et al. (2005) suggested that a magnetic reconnection episode leads to the rapid change and penumbral decay of δ sunspots associated with major flares. In these observation cases, the process of a magnetic reconnection episode is not studied clearly, such as where the magnetic reconnection episode occurs.

We find that there are no magnetic loops connecting S1 and S2 before the reconnection episodes because they emerge in different regions. This indicates that they cannot decay or disappear through a simple submergence mechanism at the same time. When the magnetic reconnection episodes begin, a set of small-scale magnetic loops form resulted from the reconnection episodes, and their footpoints are rooted in S1 and S2 (the yellow line in Figure 4). After that, flux submergence may be the principal mechanism causing the decay and disappearance of S1 and S2 accompanied by magnetic cancellation between P2 and N1 (Rabin et al. 1984). Furthermore, even if the magnetic polarity (P1) does not correspond to a sunspot, its flux can also be removed from the solar surface by a magnetic reconnection episode followed by flux submergence. However, the NVST does not obtain Dopplergrams in the chromosphere and the Dopplergrams in the photosphere obtained by the SDO have messy signals. Also, obvious redshifted features are not clearly observed in the magnetic cancellation region during this event.

Zwaan (1987) proposed two scenarios to explain magnetic flux cancellation, such as "U-loop emergence" and "Ω-loop submergence." For the first scenario, a magnetic reconnection episode occurs below the photosphere and the cancellation region has a blueshifted feature. While for the later one, a magnetic reconnection episode occurs above the photosphere and the cancellation region has a redshifted feature. Based on our observations that the magnetic reconnection episodes take place above the photosphere, we conclude that our observations are consistent with the "Ω-loop submergence" scenario.

The decay rate of the area of pore S2 is estimated to be 7.3 $Mm^2 hr^{-1}$. Previous studies found that the decay of the sunspot area is less than 4.2 $Mm^2 hr^{-1}$ (e.g., Martínez et al. 1993; Martínez Pillet 2002; Verma et al. 2018; Li et al. 2021b). In addition, the magnetic flux decay of the small pore S2 in this event (5.1×10^{19} Mx hr^{-1}) is similar to the results in previous cases whether it is related to a magnetic reconnection episode (2×10^{20} Mx hr^{-1}) (Wang 1992) or not related to a magnetic reconnection episode (around 10^{19} Mx hr^{-1}) (Martínez Pillet et al. 1997; Benko et al. 2018; Verma et al. 2018; Li et al. 2021b; Murabito et al. 2021). However, it should be noted that the pores we studied have a smaller spatial scale and a weaker magnetic field than the previous cases. Even so, we can still obtain the values, which are larger than or similar to those of big sunspots. Therefore, it is believed that a magnetic reconnection episode is an efficient mechanism of solar pore decay.

In summary, the decay and disappearance of the small pores and magnetic polarities driven by small-scale magnetic reconnection episodes are studied in detail by high-resolution observations during the development stage of NOAA AR 12778. We suggest that a magnetic reconnection episode is a crucial and effective mechanism of pore decay, especially a small-scale magnetic reconnection episode. However, observational cases are rarely reported until now, which may be directly related to the limitations of the telescope resolution and the measurement accuracy of magnetic fields on the Sun. In the future, finer structures and more accurate magnetic fields may be observed to study the relationship between small-scale magnetic reconnection episodes and sunspot decay, and we look forward to finding more similar events as well as providing detailed information about flux submergence through the high-resolution data observed by the NVST in the wings of the Hα line or other observation equipment.

ORCID iDs

Zhike Xue https://orcid.org/0000-0002-6526-5363
Xiaoli Yan https://orcid.org/0000-0003-2891-6267
Liheng Yang https://orcid.org/0000-0003-0236-2243
Jie Chen https://orcid.org/0000-0001-7472-5539
Jincheng Wang https://orcid.org/0000-0003-4393-9731
Qiaoling Li https://orcid.org/0000-0003-2045-8994

References

Asai, A., Yokoyama, T., Shimojo, M., & Shibata, K. 2004, ApJL, 605, L77
Benko, M., González Manrique, S. J., Balthasar, H., et al. 2018, A&A, 620, A191
Bobra, M. G., Sun, X., Hoeksema, J. T., et al. 2014, SoPh, 289, 3549
Bruzek, A. 1980, in Proc. IAU Symp. 91, Solar and Interplanetary Dynamics, ed. M. Dryer & E. Tandberg-Hanssen (Dordrecht: Reidel), 203
Cheng, X., Zhang, J., Saar, S. H., & Ding, M. D. 2012, ApJ, 761, 62
Gokhale, M. H., & Zwaan, C. 1972, SoPh, 26, 52

González Manrique, S. J., Kuckein, C., Collados, M., et al. 2018, A&A, 617, A55
Hannah, I. G., & Kontar, E. P. 2012, A&A, 539, A146
Harvey, K., & Harvey, J. 1973, SoPh, 28, 61
Hou, Z. Y., Tian, H., Chen, H. C., et al. 2021, ApJ, 915, 39
Lee, L. C., & Lee, K. H. 2020, RvMPP, 4, 9
Leka, K. D. 1997, ApJ, 484, 900
Lemen, J. R., Title, A. M., Akin, D. J., et al. 2012, SoPh, 275, 17
Li, Q. L., Yan, X. L., Wang, J. C., et al. 2019, ApJ, 886, 149
Li, Q. L., Zhang, L., Yan, X. L., et al. 2021a, ApJ, 913, 147
Li, T., Priest, E., & Guo, R. 2021b, RSPSA, 477, 20200949
Liu, C., Deng, N., Liu, Y., et al. 2005, ApJ, 622, 722
Liu, Z., Xu, J., Gu, B. Z., et al. 2014, RAA, 14, 705
Martínez Pillet, V. 2002, AN, 323, 342
Martínez Pillet, V., Lites, B. W., & Skumanich, A. 1997, ApJ, 474, 810
Martínez, P. V., Moreno-Insertis, F., & Vázquez, M. 1993, A&A, 274, 521
Meyer, F., Schmidt, H. U., Weiss, N. O., & Wilson, P. R. 1974, MNRAS, 169, 35
Murabito, M., Guglielmino, S. L., Ermolli, I., et al. 2021, A&A, 653, A93
Murabito, M., Romano, P., Guglielmino, S. L., & Zuccarello, F. 2017, ApJ, 834, 76
Ni, L., Ji, H., Murphy, N. A., & Jara-Almonte, J. 2020, RSPSA, 476, 20190867
Pesnell, W. D., Thomopson, B. J., & Chamberlin, P. C. 2012, SoPh, 275, 3
Petrovay, K., & Moreno-Insertis, F. 1997, ApJ, 485, 398
Rabin, D., Moore, R., & Hagyard, M. J. 1984, ApJ, 287, 404
Scherrer, P. H., Schou, J., Bush, R. I., et al. 2012, SoPh, 275, 207
Shen, Y. D. 2021, RSPSA, 477, 20200217
Shibata, K., Ishido, Y., Acton, L. W., et al. 1992, PASJ, 44, L173
Srivastava, A. K., Mishra, S. K., Jelínek, P., et al. 2019, ApJ, 887, 137

Sturrock, P. A. 1966, Natur, 211, 695
Su, Y., Liu, R., Li, S., et al. 2018, ApJ, 855, 77
Takasao, S., Asai, A., Isobe, H., & Shibata, K. 2012, ApJL, 745, L6
Tarr, L. A., Longcope, D. W., McKenzie, D. E., & Yoshimura, K. 2014, SoPh, 289, 3331
Treumann, R. A., & Baumjohann, W. 2015, A&ARv, 23, 4
van Driel-Gesztelyi, L. 1998, in ASP Conf. Ser. 155, Three-Dimensional Structure of Solar Active Regions, ed. C. E. Alissandrakis & B. Schmieder (San Francisco, CA: ASP), 202
Verma, M., Denker, C., & Balthasar, H. 2018, A&A, 614, A2
Wang, H. 1992, in ASP Conf. Ser. 27, The Solar Cycle, ed. K. L. Harvey (San Francisco, CA: ASP), 97
Wiegelmann, T. 2004, SoPh, 219, 87
Wiegelmann, T., Inhester, B., & Sakurai, T. 2006, SoPh, 233, 215
Xing, C., Cheng, X., & Ding, M. 2020, Innov, 1, 100059
Xue, Z. K., Yan, X. L., Cheng, X., et al. 2016, NatCo, 7, 11837
Xue, Z. K., Yan, X. L., Jin, C. L., et al. 2019, ApJL, 874, L27
Xue, Z. K., Yan, X. L., Yang, L. H., et al. 2018, ApJL, 858, L4
Xue, Z. K., Yan, X. L., Yang, L. H., et al. 2020, A&A, 633, A121
Xue, Z. K., Yan, X. L., Yang, L. H., et al. 2021, ApJ, 915, 17
Xue, Z. K., Yan, X. L., Yang, L. H., Wang, J. C., & Zhao, L. 2017, ApJL, 840, L23
Yamada, M., Kulsrud, R., & Ji, H. 2010, RvMP, 82, 603
Yan, X. L., Liu, Z., Zhang, J., & Xu, Z. 2020, ScChE, 63, 1656
Yan, X. L., Yang, L. H., Xue, Z. K., et al. 2018, ApJL, 853, L18
Yokoyama, T., Akita, K., Morimoto, T., Inoue, K., & Newmark, J. 2001, ApJL, 546, L69
Zwaan, C. 1987, ARA&A, 25, 83